# Thermal Conductivity of 3D-Printed Block-Copolymer-Inspired Structures

Omar Taleb[a,b,€], Matthew Jutkofsky[a,b,€], Ryan Measel[a,b], Michael Patrick Blatt[a,b], Nadim S. Hmeidat[c], Philip R. Barnett[d], Hilmar Koerner[e], Daniel Hallinan Jr.[a,b,*]

[a] Department of Chemical and Biomedical Engineering, Florida A&M University-Florida State University College of Engineering, Tallahassee, FL 32310, USA
[b] Aero-propulsion, Mechatronics, and Energy Center, Florida A&M University-Florida State University College of Engineering, Tallahassee, FL 32310, USA.
[c] Manufacturing Science Division, Oak Ridge National Laboratory, Knoxville, TN 37932, USA
[d] University of Tennessee-Oak Ridge Innovation Institute, University of Tennessee, Knoxville, TN 37996, USA.
[e] Air Force Research Laboratory, Materials and Manufacturing Directorate, AFRL/RX, Wright-Patterson Air Force Base, Ohio 45433, USA.

[€] These authors contributed equally to this work.
[*]Author to whom correspondence should be addressed, dhallinan@eng.famu.fsu.edu

**Keywords**: Heat conduction, Thermal conductivity ratio, Morphology, Tortuosity, 3D Printing

# Abstract

This study primarily focuses on examining the impact that geometric structure has on thermal conductivity of multi-phase constructs in different 3D-printed poly(lactic acid), PLA, samples. The investigated structures are inspired by morphologies formed by diblock copolymers: lamellae, hexagonally packed cylinders, and gyroid. This research also investigates how volume percentage and material combination influence the thermal conductivity of these structures. The samples can be tailored to simulate various thermal management structures observed in practical applications, such as thermal interface materials in electronic devices. Thermal conductivity ratio is controlled using air, the least conductive material at 0.026 W/(m K), PLA at 0.136 W/(m K), and thermal paste at 5.11 W/(m K). Different models were tested against thermal conductivity measurements in order to capture the effect of material type (PLA-Air versus PLA-Thermal Paste), volume percentage, structure, and orientation. Simple, effective medium models were good predictions of thermal conductivity in lamellar structures, but it was necessary to develop models for conduction through cylindrical and gyroid structures. Finally, all results were normalized to find a universal model that is independent of structure and material. This approach provides a simple method to predict how to reduce or enhance transport properties and heat management capabilities of 3D printed objects.

# 1. Introduction

Thermal conductivity is important in various applications, such as thermal heat management, in which the rate and direction of thermal conduction must be controlled [1]. Advancements in material design principles and material fabrication have been motivated by the need to achieve sufficient thermal conductivity while also preserving other essential, application-specific properties. Technological advancement of microelectronics/semiconductors [2], automobiles [3], lithium ion batteries (LIBs)/electric vehicles [4], and heating/cooling technology [5] requires lightweight materials with excellent thermal conductivity, processability, and chemical/mechanical stability [6]. The heat generated from integration of high power chips, wireless charging, and Bluetooth® into electronic equipment reduces stability, reliability, and service life [7, 8]. LIBs are also sensitive to temperature. Heat is generated in batteries and electronics due to Joule heating, solar flux, exothermic reactions, etc. [1]. In order to prevent thermal degradation, advanced materials with desired properties (i.e. high/low thermal conductivity and mechanical strength) are essential for thermal management to increase performance, life cycle, and reliability of these systems [9, 10]. A major challenge is designing advanced lightweight materials with high thermal conductivity. Energy efficiency of portable and transportation applications greatly benefits from reduced weight. Moreover, advanced thermal control, for example, to isolate a shorted cell in a battery pack and rapidly dissipate generated heat is essential to prevent consequences, such as catastrophic thermal runaway that would threaten human life and lead to equipment failure and accidental fire [4]. This is why it is important to understand thermal conductivity of structured materials to create new ways of dealing with these heat flow issues.

A powerful way to realize essential material properties is by combining multiple phases to form a composite. Many studies have utilized polymer composites to achieve a wide range of desired properties [11-13], but challenges related to particle agglomeration, processing, and control of heat flux directionality remain. Block copolymers (BCPs) are an example of a single-component composite that is not prone to agglomeration and is readily processable. BCPs contain chemically distinct monomers (2 or more) that are grouped in multiple blocks connected along a polymer chain. Under specific conditions, BCPs microphase separate into a specific structure: lamellar, cylindrical, gyroid, or spherical. The structure that a particular BCP forms depends on the volume fraction of each block, degree of polymerization, and Flory-Huggins interaction parameter. BCP ordering and phase behavior have been well studied [14-17]. The impact of their structure has also been investigated extensively in relation to ion transport [18-22], but heat transport has received only limited attention [23, 24].

BCP alignment is useful for various applications, which includes the ability to direct flux due to anisotropic transport parameters that emerge in ordered materials [25-31]. There are multiple ways to align the structure of a BCP, for example by applying external fields such as mechanical, electrical, and magnetic [18]. Mechanical alignment is applied to thick BCP membranes via compression, extrusion, fiber drawing, roll casting, and shear [18, 32-38]. Electric and magnetic fields are powerful due to the ability to direct alignment via the orientation of the material in the field without direct material contact [18]. However, they do require that the structure be kinetically trapped, e.g. by cooling, before removing the applied field. Magnetic field alignment has the added benefit of avoiding dielectric breakdown. Motivated by the potential benefits of BCPs, this work examines aligned structures with the minority phase continuous in at least one dimension.

The use of 3D-printing has allowed for complex geometries to be created and tested. By understanding the thermal conductivity of 3D-printed materials, we can better optimize the properties of printed elements in thermal applications. Applications of particular interest that benefit from 3D printing are (1) managing pulsed heat loads with phase-change material incorporated via additive manufacturing [39-41], (2) solar thermal applications such as evaporators [42], and (3) thermoelectrics [43, 44]. There has been some work on the effect of infill percentage in simple grid structures on thermal conductivity [45-47], as well as examination of longitudinal and transverse thermal conductivity in simple grid structures [48, 49]. However, there have been few examinations of thermal conductivity in complex porous structures formed with 3D printing [50-52]. Closed-cell insulation material formed with 3D printing has been studied to determine how the geometry of a structure affects its ability to conduct heat [53]. A nacre-inspired structure has also been investigated [54]. In this study, we report thermal conductivity in block-copolymer-inspired structures. 3D-printed poly(lactic acid) (PLA) structures, with varying volume percentages and phase-contrast materials are examined and their thermal conductivity compared to different analytical models.

PLA-based composites have been extensively studied due to many useful properties such as biocompatibility, biodegradability, and shape-memory effects [55-57]. The process of choosing a material to enhance thermal properties must also consider the impact on other properties, such mechanical strength. Some commonly used additives are graphene, carbon nanotubes, and metal particles [58]. Rather than focusing on the design of composite materials, in this study multiple homogeneous materials are combined in macroscopic structures formed via 3D printing. Infill percentage is a common term in fused filament fabrication (FFF) that refers to the volume fraction that the printed filament occupies. It is common for 3D-printed materials to have hollow regions that reduce printing time and material usage. Air is typically present in these hollow regions, but it is possible to fill the structure with other materials to alter thermal properties. By creating structures with different material combinations, it is possible to examine how thermal conductivity ratio affects the thermal conductivity of the structure. With multiple materials present, we will refer to volume percentage of each material rather than infill percentage to avoid ambiguity. Creating a high contrast between PLA thermal conductivity and the thermal conductivity of the additive can lead to interesting results and aid in the design of 3D-printed structures and polymer composites designed for specific goals, such as directing heat flow.

Morphological structures that commonly occur in microphase separated BCPs include hexagonally packed cylinders, lamella, and gyroid. The cylinders comprise the minority block, which we refer to as A, in a matrix of the majority block, referred to as B. Within an ordered grain of coherent orientation, the cylinders are continuous in only one dimension. Lamellar morphology comprises alternating flat microdomains of A and B. Within an ordered grain, the lamellae are continuous in two dimensions. Flat layered samples are relevant to existing applications like surface coatings and heat transfer fins. Gyroid is an intriguing structure in which both A and B phases are continuous in three dimensions. It offers unique insight into the degree to which structure can influence heat flow since the interface between the blocks is continuous and forms a complex, periodic surface with high surface area. This work reports a systematic investigation of macroscopic structures that mimic the microscale morphologies seen in BCPs. The macroscopic structures are well controlled and easy to characterize in coordinate directions without thermal boundary layers complicating measurement accuracy, as has been seen in self-assembled BCP thin films of lamellar structures [59]. Moreover, the thermal conductivity of each phase is readily modified. This work on model systems generates fundamental understanding to aid additive manufacturing design of porous structures.

Extrapolation of this understanding to smaller scale may provide insight into composite material properties. The purpose of this study is to investigate thermal conductivity of different structures on a 3D-printed prototype level. Key variables that are investigated are the type of structure (lamellar, gyroid, and cylindrical), as well as the thermal conductivity ratio and volume percentage of each phase.

# 2. Experimental Section

### 2.1 Sample Preparation

All samples were printed using FFF with PLA filament (MakerBot) and were designed with equally spaced features to form 40 mm cubes with volume fractions between 10% and 100% PLA. Three structures were studied, lamellar, cylindrical, and gyroid. These structures are shown in Table 1 for 25% PLA samples. The isometric view shows three faces of the cubes, while the back view shows the cube faces that were in contact with the transient-method sensor for measurements in parallel orientation (see below for more detail). The technical drawings of each structure that were used to generate 3D printer commands are shown in Table S1.

Table 1. High-resolution photographs of 3D-printed PLA samples with 25% PLA by volume. All 3 structures studied are shown from 2 different perspectives on a 3 mm grid.

| Structure | Isometric View | Back View |
|---|---|---|
| **Lamellar** | 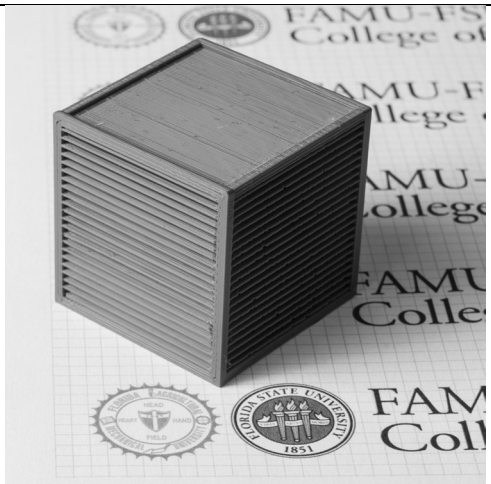 | 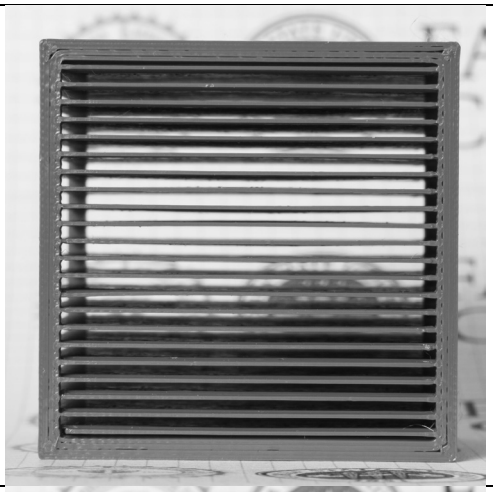 |
| **Cylindrical** | 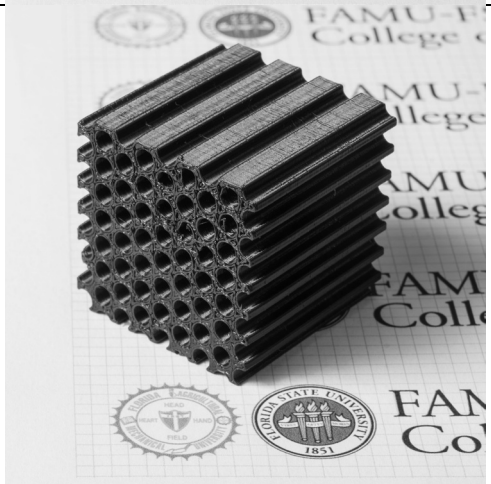 | 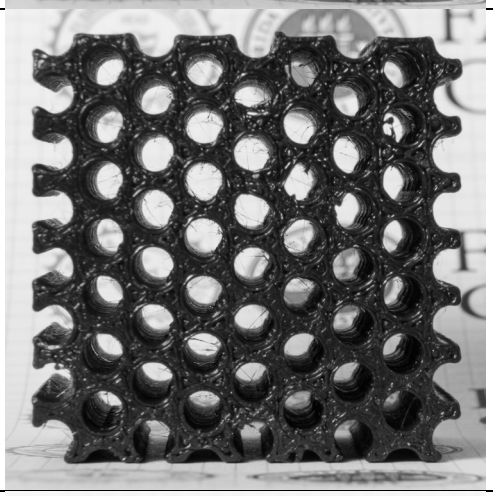 |
| **Gyroid** | 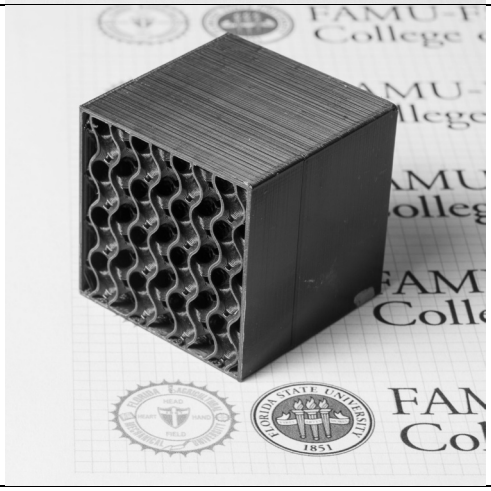 | 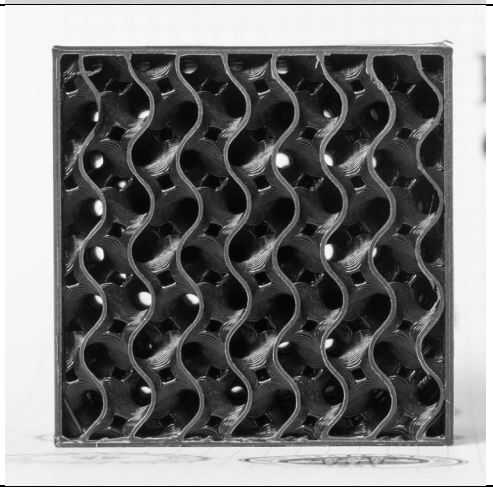 |

Lamellar structures had equally spaced fins (one print road width of approximately 0.45 mm thickness) to form 40 mm cubes with PLA volume fractions of 10%, 25%, 50% and 75%. Volume fraction was controlled by modeling the number of fins in the input file and setting their width equal to a single print road width (Autodesk Fusion 360). A solid frame of 2.0 mm thickness was modeled to support the fins on all edges of the cubes. The structures were sliced using Prusa Slicer 2.5 and printed on a Prusa MK3S using a 0.4 mm nozzle with nominal layer thickness of 0.15 mm, nozzle temperature of 215 °C, and bed temperature of 60 °C. A brim was added to the material to enhance adhesion to the polyetherimide build plate and removed after printing.

A 2D model was used to design the hexagonally packed cylindrical structure that were created in 40 mm cubes. Circles were placed at the vertices of equilateral triangles, which were connected to form trapezoids as shown in Figure 1. For PLA volume fraction, $\phi_{PLA} = 0.5$, a lattice area contains equal areas of circle (eq. 1, lefthand side) and matrix (eq. 1, righthand side).

$$\frac{3}{6}\pi R^2 = \frac{1}{2}BH - \frac{3}{6}\pi R^2 \text{ (eq. 1)}$$

Using the Pythagorean theorem, height, $H$, can be expressed in terms of base length, $B$ (equation 2). This can be substituted into equation 1, yielding equation 3.

$$H = \left(\frac{3}{4}\right)^{1/2} B \quad \text{(eq. 2)}$$

$$\mathrm{B} = \frac{(4\pi)^{1/2}}{3^{1/4}}\mathrm{R} \quad \text{(eq. 3)}$$

By fixing the circle radius to 3.5 mm, the lateral distance between center points of the circles, $B$, can be calculated using equation 3 and the vertical distance between rows, $H$, is also known (equation 2).

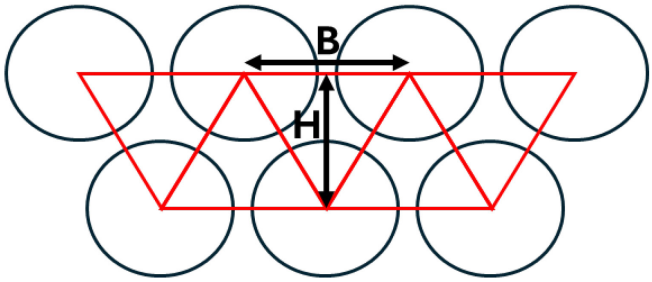


Figure 1. 3D printing design of cylindrical structure, cylinders on a hexagonal lattice.

A general formula for any volume percentage can be written in terms of the PLA volume fraction. Equation 5 is found by combining equations 2 and 4 and solving for B.

$$\phi_{\mathrm{PLA}} = 1 - \left(\frac{\pi R^2}{BH}\right) \quad \text{(eq. 4)}$$

$$\mathrm{B} = \left(\frac{2\pi}{(1-\phi_{PLA})\sqrt{3}}\right)^{1/2} R \quad \text{(eq. 5)}$$

Using the design described above, PLA volume percentages of 25%, 50%, and 75% were created in 40 mm cubes. Due to lack of structural integrity, 10 vol% PLA cylindrical samples were not studied. The cylinders were placed as cuts in Fusion 360, and the cubes were exported for FFF 3D printing using Ultimaker Cura to slice G-code and printed using MakerBot PLA filament. The structures were printed on a Creality Ender 5 plus using a 0.4 mm nozzle with nominal layer thickness of 0.15 mm, nozzle temperature of 215 °C, and bed temperature of 60 °C. A skirt was added to the material to enhance adhesion to the glass build plate.

Gyroid is a continuous structure offering unique thermal properties. Gyroid samples were created by making a solid 40 mm cube in Fusion 360. The solid cube was put into Cura, where this software has a built-in design of gyroid structure. PLA volume percentages of 10%, 25%, 50%, and 75% were created. The top and bottom layers were set to 0 to allow the gyroid structure to extended to the top and bottom of the cube for testing. The G-code was exported to an FFF 3D printer, printing MakerBot PLA filament to create the various samples. The structures were printed on a Creality Ender 5 plus using a 0.4 mm nozzle with nominal layer thickness of 0.15 mm, nozzle temperature of 215 °C, and bed temperature of 60 °C. A skirt was added to the material to enhance adhesion to the glass build plate.

In heterogeneous structures, the material filling the porous regions can significantly influence the overall thermal conductivity of the 3D-printed object and thereby heat transport. As shown in Table 1, we refer to the ratio of thermal conductivity of the more conductive phases to that of the less conductive phase as thermal conductivity ratio. In this study, air and thermal paste are used to fill the porous regions of the PLA structures, shown in Table 1. 3D-printed PLA has a thermal conductivity of 0.136 $\frac{\mathrm{W}}{\mathrm{m\,K}}$ [60, 61], air has a thermal conductivity of 0.026 $\frac{\mathrm{W}}{\mathrm{m\,K}}$ [62], and thermal paste has a thermal conductivity of 5.11 $\frac{\mathrm{W}}{\mathrm{m\,K}}$. For the PLA-Air system, the PLA volume percentages investigated for lamellar, cylindrical, and gyroid structures are all shown in Table 2. The samples that contained thermal paste were created by manually inserting the paste into the porous regions of the samples. The viscosity of the paste was high enough that all gaps were completely filled. As shown in Table 2, lamellar samples were tested with thermal paste at 10%, 25% and 50% volume of PLA. The 75% volume of PLA samples were not studied with thermal paste, because it could not be inserted into the fine air gaps of the samples. Cylindrical samples with thermal paste were studied at PLA volume percentages of 25%, 50%, and 75%. Gyroid samples were not studied with thermal paste due to their inherently complex geometry preventing infiltration of the paste. Both PLA-Air and PLA-Thermal Paste systems were tested in parallel and in series orientations, and these results were compared to theoretical predictions as well as to other literature.

Table 2. Summary of the PLA volume percentages and thermal conductivity ratios studied in different structures.

| | | Thermal conductivity ratio | |
|---|---|---|---|
| | | $k_{PLA}/k_{Air}$ | $k_{paste}/k_{PLA}$ |
| | | 5 | 37.5 |
| PLA vol% | 10% | Lamellar | Lamellar |
| | | Gyroid | |
| | 25% | Lamellar | Lamellar |
| | | Cylindrical | Cylindrical |
| | | Gyroid | |
| | 50% | Lamellar | Lamellar |
| | | Cylindrical | Cylindrical |
| | | Gyroid | |
| | 75% | Lamellar | |
| | | Cylindrical | Cylindrical |
| | | Gyroid | |

## 2.2 Thermal Conductivity Measurements of Different Structures

### *2.2.1 Transient Method*

Transient thermal conductivity was measured with a C-Therm Technologies Ltd., Trident Thermal Conductivity Instrument, employing a Modified Transient Plane Source (MTPS) method. In this method, temperature is measured as a function of time after a pulse of known thermal power has been applied. The guard ring ensures that transport is 1D, allowing for thermal conductivity to be determined from a fit to the 1D transient temperature data. To ensure consistency in temperature and humidity conditions during the measurement process, the MTPS sensor is placed in a humidity chamber. The chamber is set to 50% humidity and 25 °C. Multiple measurements were conducted over several minutes, enabling the monitoring of potential irregularities and increasing the precision of the obtained readings. The samples were tested in two different orientations relative to the heat source: series and parallel, as shown in Figure 2. The naming convention originates from how the thermal resistance of each phase is arranged with respect to the heat vector produced by the MTPS. In other words, the thermal resistance of each phase is in parallel when an axis of symmetry of the structure is parallel to the heat flux, whereas thermal resistances are in series when the axis (or axes) of symmetry are perpendicular to the heat flux direction.

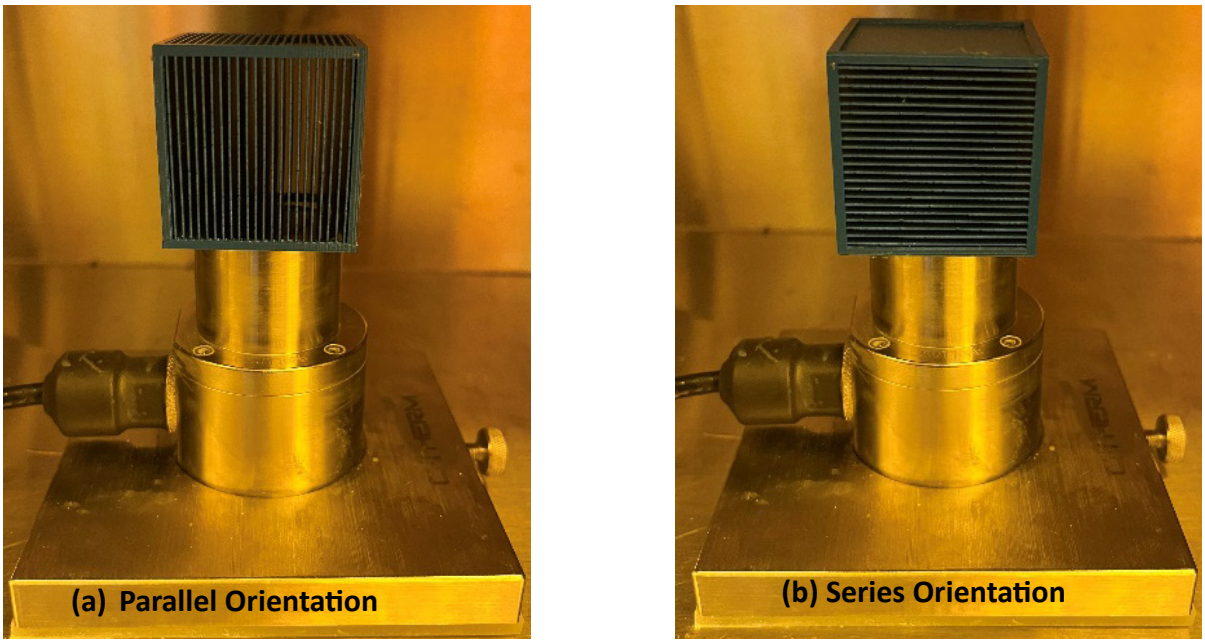


Figure 2. 25% infill sample placed on the C-Therm MTPS sensor ready to be tested **(a)** in parallel orientation and **(b)** in series orientation.

*2.2.2 Steady-State Method*

The series-oriented samples were also tested with a different technique that utilized a heat source to achieve a heat flow at steady state and multiple thermocouples; see Figure 3. This second technique was developed to address a shortcoming of the transient method, whereby transient thermal conductivity data exhibited no change when the system was changed from PLA-Air to PLA-Thermal Paste. This drastic material property change should have elicited a major shift in the samples' overall thermal conductivity. More details about the limitation of the transient method, which is related to heat penetration depth, are discussed in the results and discussion section.

The steady-state experiment comprised an insulative layer of 1-inch-thick polyurethane foam that enveloped the sample from all sides except the bottom surface, as depicted in Figure 3. The bottom surface contacted a heated plate, which served as the heat source. Thermocouples were positioned on each side of the sample, placed between the insulation and the sample itself, to ensure that the insulation prevented natural convection. Additionally, thermocouples were inserted at the bottom, middle, and top of the sample, between the PLA gaps, to monitor heat flow. Thermocouple data was logged every 0.5 seconds to a computer via an eight-channel temperature/voltage input USB data acquisition module from Omega. The experiment ended once the three thermocouples inside the sample reached a steady-state temperature.

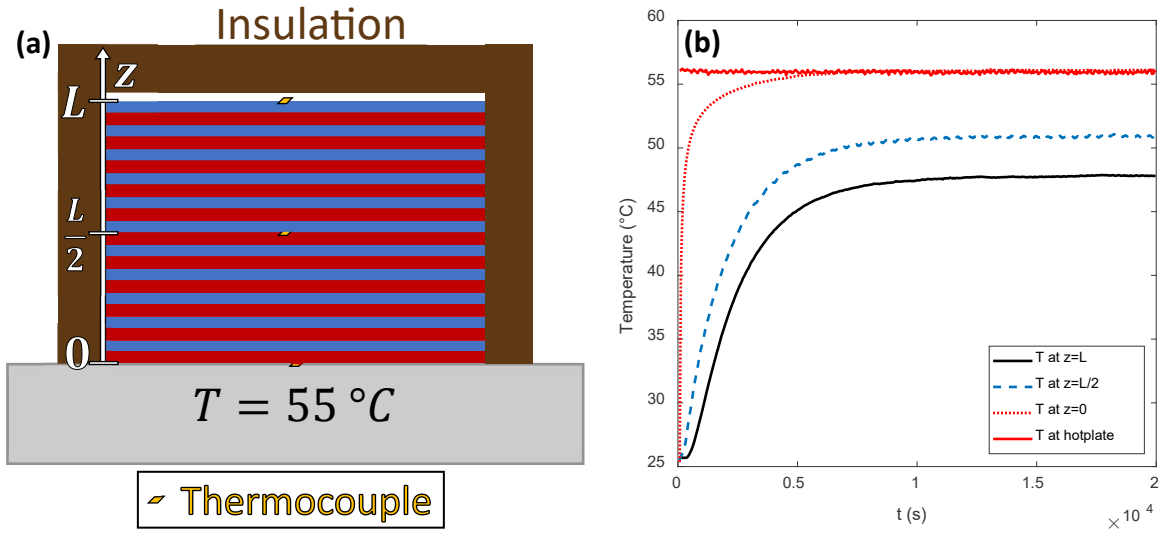


Figure 3. **(a)** Schematic of experimental set-up for measurements in series configuration that we term steady-state measurements. **(b)** Representative experimental data from an experiment. The experiment was calibrated with a dense sample of known thermal conductivity. Then, the data at $z = L$ was used to determine the thermal conductivity of samples with unknown thermal conductivity.

The partial differential equation (PDE) that describes heat transfer through the sample during steady-state measurements is shown in equation 6.

$$\frac{\partial T(t,z)}{\partial t} = \alpha \frac{\partial^2 T(t,z)}{\partial z^2} \quad \text{(eq. 6)}$$

Thermal diffusivity is $\alpha = \frac{k}{\rho C_p}\left(\frac{\text{m}^2}{\text{s}}\right)$. With the boundary and initial conditions expressed below, a solution can be found that fits the temperature profiles shown in Figure 3.

Constant temperature boundary condition: $T(t,0) = 55$ °C at $z = 0$
Flux matching of conduction in cube and convection from cube surface: $-k\frac{dT}{dz} = h(T - T_\infty)$ at $z = L$
Constant temperature initial condition: $T(0,z) = 25$ °C at $t = 0$

$T$ is temperature, $T_\infty$ is ambient temperature, $t$ is time, $z$ is the spatial coordinate, $k$ is thermal conductivity, $h$ is convective heat transfer coefficient, $L$ is the height of the cube, $\rho$ is the density of the cube, and $C_p$ is the specific heat of the cube. The solution of the PDE is in the form of a Fourier series, equation 7. Refer to the Supporting Information for derivation of equation 7.

$$T = T(0,z) + (T(t,0) - T(0,z))\left[\frac{-\beta}{1+\beta}\frac{z}{L} + 1 - \sum_n \frac{4}{2\lambda_n - \sin(2\lambda_n)} e^{-\lambda_n \frac{\alpha}{L^2} t} \sin\left(\lambda_n \frac{z}{L}\right)\right] \quad \text{(eq. 7)}$$

$\lambda_n$ are the eigenvalues of the basis function, and the Biot number is $\beta = \frac{hL}{k}$. Equation 7 was fit to the data by varying $\alpha$ and $\beta$. Then, $\beta$ was used to calculate the thermal conductivity, $k$. The steady-state solution

from solving the boundary value problem with the time derivative set to zero, $\frac{T_{ss}-T(0)}{T_\infty-T(0)}=\frac{\beta}{1+\beta}\frac{z}{L}$, was also used to determine $\beta$ from steady-state temperatures alone. In either case, the process for calibrating the experiment is as follows. A dense PLA cube of the same size was printed (i.e. 100% PLA), and its $k$ was evaluated using the transient method. Then the steady-state measurement was conducted on this sample, and the calculated $\beta$ was used to find the convective heat transfer coefficient, $h$. This was then used to determine $k$ from steady-steady measurements on lamellar, cylindrical, and gyroid structures.

# 3. Results and discussions

## 3.1 Lamellar and Cylindrical

### *3.1.1 Parallel orientation*

The first system tested was PLA-Air with a thermal conductivity ratio of $k_{PLA}/k_{Air}=5$. This is the lower thermal conductivity ratio system studied in this work. The structural component is PLA with a higher thermal conductivity of 0.1364 W/(m K), measured with the transient method. Figure 4 (a) shows measured thermal conductivity versus PLA volume percentage for both the lamellar and cylindrical structures. These results were obtained with the transient method and are tabulated in Table S2. A theoretical prediction based on parallel heat conduction, equation 9, is also presented in Figure 4 (a).

The theoretical approach to transport of heat through BCP-inspired structures can be approached with equations that describe series and parallel conduction. Series conduction takes place through both phases, and effective thermal conductivity, $k_{series}$, is a weighted harmonic average based on volume fraction [23].

$$k_{series}=\left(\frac{\phi_A}{k_A}+\frac{\phi_B}{k_B}\right)^{-1} \quad (\text{eq. } 8)$$

The volume fractions of phases A and B are represented by $\phi_A$ and $\phi_B$, respectively. The thermal conductivities of phases A and B are symbolized as $k_A$ and $k_B$, respectively. In the case of parallel conduction, both phases can conduct heat simultaneously, and the effective thermal conductivity is determined using a basic rule of mixtures [23].

$$k_{parallel}=k_A\phi_A+k_B\phi_B \quad (\text{eq. } 9)$$

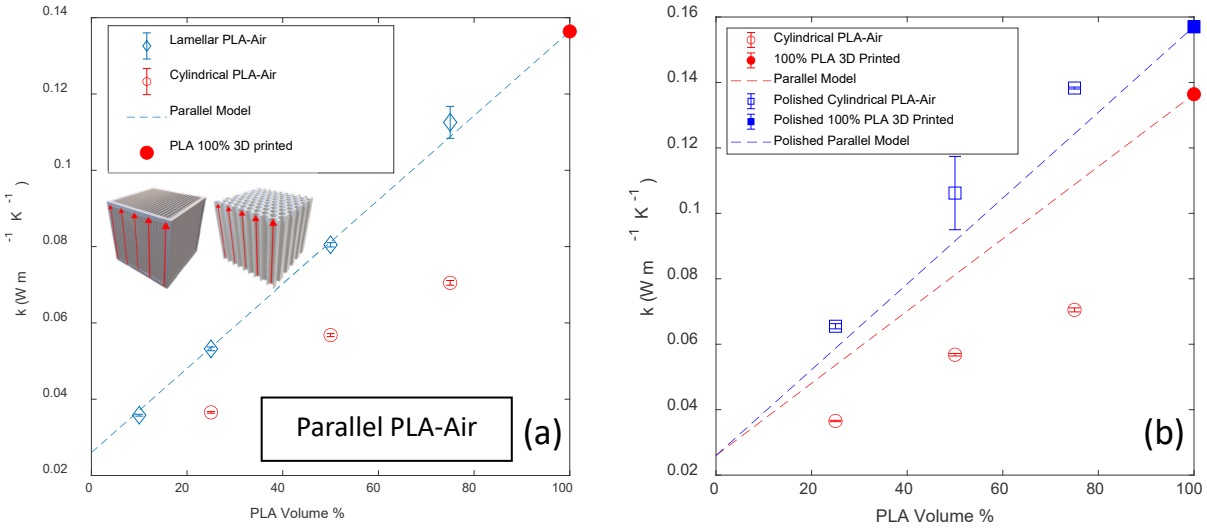


Figure 4. (a) Thermal conductivity (measured with the transient method) of lamellar and cylindrical structures of the PLA-Air system as a function of PLA volume percentage in parallel orientation to the heat source. Error bars are one standard deviation. Dashed line is the parallel model (equation 9). Inset shows sample orientation with red arrows that denote direction of heat flux. (b) Thermal conductivity from the transient method as a function of PLA volume % for hexagonally packed cylindrical samples in parallel orientation (open symbols) and dense, 3D-printed PLA (filled symbols) as printed (○) and with polished surfaces (□). The parallel model (equation 9) is shown as dashed lines, in which the as-printed or polished 100% PLA thermal conductivity is used to generate the model. This figure shows that the anomalously low thermal conductivity of cylindrical samples is due to inordinately higher roughness as compared to other 3D-printed structures. The roughness of cylindrical samples was also detected by physical inspection. All other reported data is for as-printed samples.

As Figure 4 (a) demonstrates, the experimental results for lamellar samples were observed to closely align with the predictions of the theoretical model. This alignment suggests that the thermal conductivity of these structures is well-predicted by theoretical calculations, indicating the reliability of the model for estimating the thermal performance of infill materials for the lamellar configuration. Conversely, the thermal conductivity of the cylindrical structure is overpredicted by theoretical prediction. It was noted that the cylindrical structure exhibited a rougher surface after 3D printing than other samples (see back view in Table 1). In order to examine if this was the cause of the anomalously low thermal conductivity, the surface was polished smooth (see front face in isometric view of Table 1) and thermal conductivity was measured again. As shown in Figure 4 (b), polished cylindrical samples exhibit considerably higher thermal conductivity that more closely agree with the parallel model. Polishing resulted in a much more significant increase of cylindrical-sample thermal conductivity than other structures, pointing to the challenge of forming small radii of curvature with FFF. For example, the 75% PLA cylindrical sample increased from 0.071 W/(m K) as printed to 0.138 W/(m K) polished, whereas thermal conductivity of the dense cube increased from 0.136 W/(m K) as printed to 0.157 W/(m K) polished. Our values agree well with those reported in literature: 0.13 W/(m K) for 3D-printed PLA and 0.16 W/(m K) for PLA filament [60, 61]. Throughout the remainder of this work, only as-printed values are reported.

Additional measurements were done using a highly conductive thermal paste in place of air. The significantly larger thermal conductivity of thermal paste, 5.11 W/(m K), as compared to air, 0.026 W/(m K), made it possible to switch which part of the structure was more conductive and to change the thermal conductivity ratio from $k_{PLA}/k_{Air} = 5$ to $k_{paste}/k_{PLA} = 36$. The thermal conductivities of these samples are reported in Figure 5. The values of the data in Figure 5 are reported in Table S3. Also shown in Figure 5 is the parallel model, equation 9. The good agreement between the experimental and theoretical results for the lamellar samples can be attributed to the simplicity and inherent regularity of this structure. The theoretical prediction of cylindrical structure thermal conductivity overpredicted that of PLA-Thermal Paste, as was observed for PLA-Air. This is surprising because the presence of thermal paste was expected to mitigate experimental error in the PLA-Air system that could have been present due to surface roughness and heat convection. The parallel model overpredicting effective thermal conductivity in both cases indicates that the disagreement between theory and experiment may be inherent to the cylindrical structure itself. We speculate that experimental uncertainty could result from the increased complexity of the cylindrical structure. For example, curvature of the interface could have an effect. Moreover, the lateral placement of the sample on the sensor can affect which parts of the hexagonal packing are sampled.

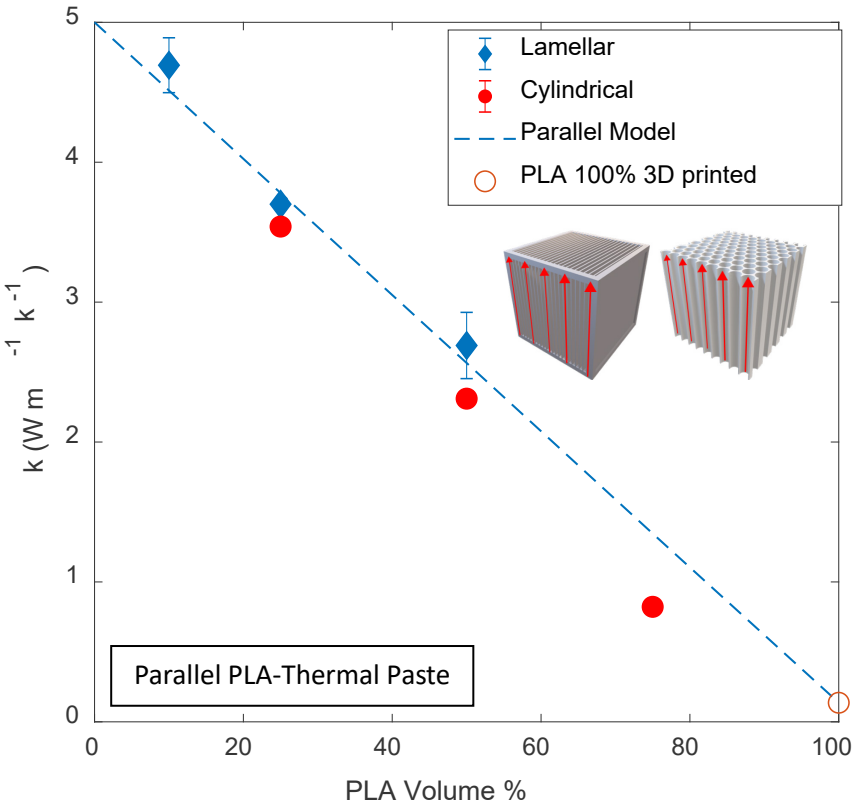


Figure 5. Thermal conductivity of lamellar and cylindrical structures filled with thermal paste, $k = 5\ \mathrm{W/(m\ K)}$, as a function of PLA volume percentage in a parallel orientation to the heat source. Error bars are one standard deviation; those of cylindrical samples are smaller than the data points. Inset shows sample orientation with red arrows that denote direction of heat flux.

*3.1.2 Perpendicular orientation.*

Transient tests were performed in perpendicular orientation, as shown in Figure 2 (b). Figure S2 shows the effect of lamellar PLA volume percentage, with equation 8 used as theoretical prediction for these values. The thermal conductivity was higher than the prediction at 10%, 25%, and 50%. Thermal conductivity increased with increasing PLA volume percentage from 10% to 50%; at 75% volume of PLA the thermal conductivity dropped to below that at 10% volume of PLA. The 75% thermal conductivity is closer to the theoretical prediction. Due to these anomalous results, the PLA layer thickness at each volume percentage was measured and is reported in Figure S3. The PLA layer thickness in the lamellar structure decreased from 0.46 mm to 0.27 mm with increasing percentage of PLA volume from 10% to 75%. So, the effect of air in a series experiment cannot be detected if the thickness of the first layer is higher than 0.27 mm. It is found that the transient method does not yield accurate effective thermal conductivity values in series orientation, where the thickness of the first layer dominates the measurement.

Due to the limitation of the transient method in measuring the thermal conductivity of the perpendicular orientation, a steady state experiment, described in the experimental section and shown in Figure 3, was used to evaluate the thermal conductivity of the series orientation. Figure 6 shows temperature profiles for a dense cube. A dense PLA cube is used for calibration of the experiment, where its thermal conductivity, $k$, measured with the transient method is 0.1364 W/(m K). The parameters $\alpha$ and $\beta$ were adjusted to regress the model to the data collected at $z = 1$ (where 2 thermocouples are attached). The Biot number, $\beta = \frac{hL}{k}$, is used to find $h$ since all other parameters are known in this case. This $h$ is assumed to be constant and is used in evaluating the thermal conductivity $(k)$ in the rest of the structures since the same conditions are applied. The dense cube experiment is averaged over 3 collected experiments.

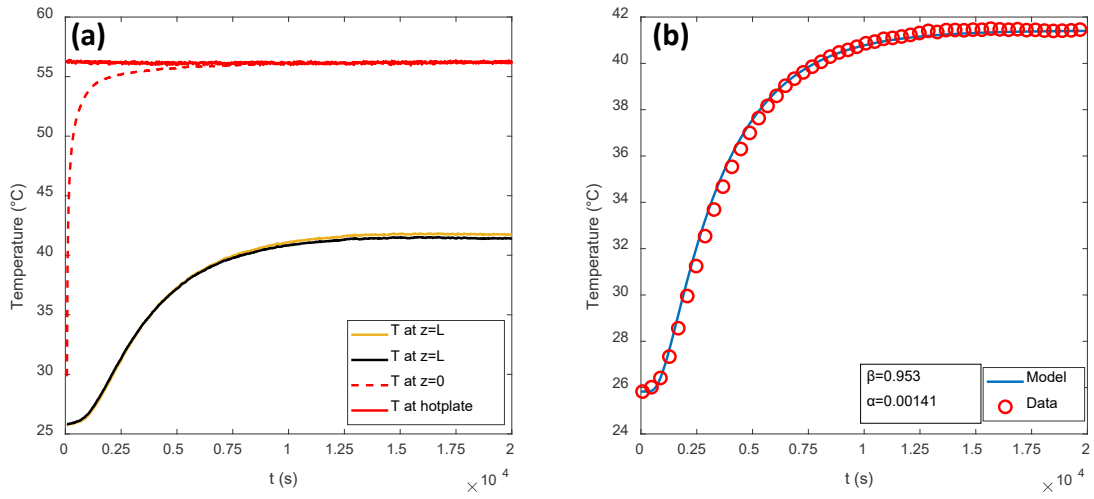


Figure 6. **(a)** Representative result of a calibration experiment for the steady-state method using a dense, 3D-printed, PLA cube. **(b)** Results of fitting $\alpha$ $(\mathrm{cm}^2/\mathrm{s})$ and $\beta$ to the temperature profile at $z = L$ for the dense PLA cube. Data from each thermocouple at $z = L$ was fit and the results from three measurements were averaged and are reported in Table 3 and Table S4.

A parametric study of how the model changes with $\alpha$ and $\beta$ is shown in Figure S4. Figure 6(b) shows the best fit of the model to a representative steady-state calibration measurement. It is worth noting that $\beta$ can be calculated from equation 10 that comes from the steady solution at $z = L$ or found from regression to the full transient data set; both methods lead to the same value of $\beta$, which is an indication that conduction is the dominant heat transport mechanism within the block.

$$\beta = \frac{T(\infty, L) - T(t, 0)}{T(0, z) - T(\infty, L)} = \frac{hL}{k} \quad \text{(eq. 10)}$$

The value calculated from equation 10 was averaged over both thermocouple measurements at $z = L$ in a total of 3 experiments. This value was then used to calculate $h$, which is the heat transfer coefficient that quantifies convection from the top of the cube through the small air gap to the insulation and subsequent heat loss through the imperfect insulation. This $h$ is expected to be the same in all the perpendicular experiments. This $h$ was then used to find the thermal conductivity, $k$, in series structures.

Table 3. Calibration values for model parameters used to analyze steady-state data. $\beta$ was calculated from initial, final, and bottom temperatures measured with the steady-state method as shown in Equation 10. The value of $k$ for the 100% PLA cube, measured with the transient method, was used to find the heat transfer coefficient, h.

| Parameter | Calibrated Value |
|---|---|
| $\beta$ | $0.85 \pm 0.07$ |
| $k \left[\frac{\mathrm{W}}{\mathrm{m\ K}}\right]$ | $0.1364 \pm 0.0008$ |
| $h \left[\frac{\mathrm{W}}{\mathrm{m^2\ K}}\right]$ | $2.90 \pm 0.24$ |

The steady-state method was used to evaluate the thermal conductivity of each structure and material combination. In the series experiments, the cylindrical structure has 2 orientations, shown in Figure 7. The first orientation is when the heat flux is in the q-direction; the second one is when the heat flux is in the r-direction. These directions are defined by the hexagonal close-packed cylindrical structure. Table S4 reports $\alpha$ and $\beta$ for all the structures and material combinations studied in this paper. As mentioned previously, the thermal conductivity is calculated from $\beta$. Representative steady-state measurements of structured samples are shown in Figure 8 and S5-S7, along with best fits of the analytical solution (equation 7) to the data collected. Thermal conductivity values from the steady-state series experiments are shown in Figure 9. In the PLA-Thermal Paste system, the cylindrical structure in r-direction orientation showed the highest thermal conductivity of 0.308 W/(m K), followed by lamellar structure of 0.221 W/(m K), and finally the cylindrical structure in q-direction with 0.187 W/(m K). These results demonstrate the importance of orientation and how it can play a key role in increasing or decreasing thermal conductivity.

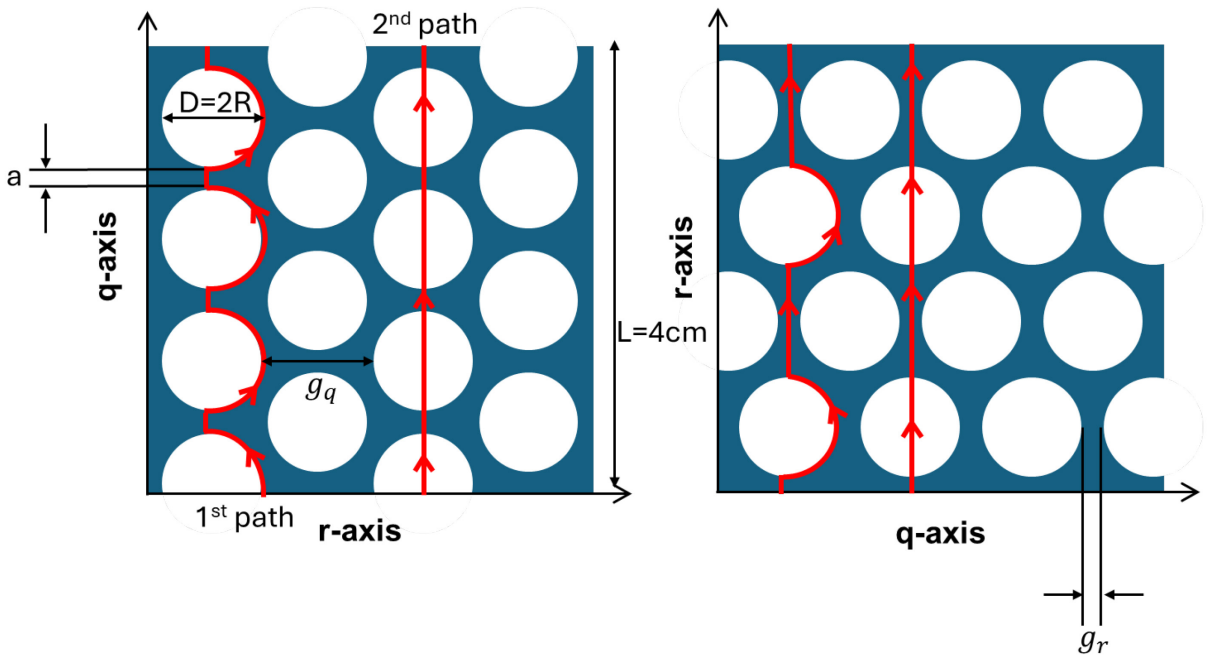


Figure 7. Schematic of coordinate directions of cylindrical structure in series orientation with dimensions and heat flux pathways noted.

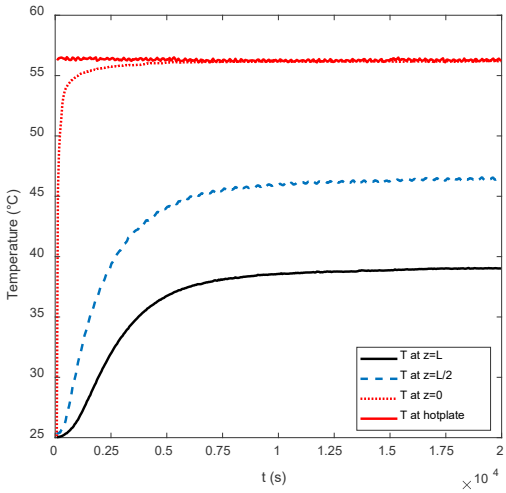


**(a)** Cylindrical q-direction PLA-Air

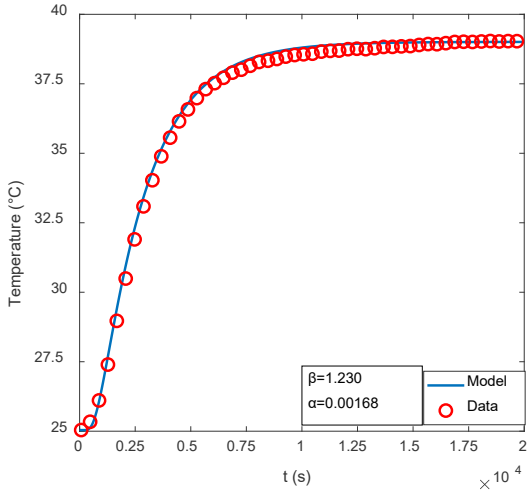


**(b)** Cylindrical q-direction PLA-Air

Figure 8. **(a)** Temperature versus time for cylindrical PLA-Air sample in the q-direction of series orientation. **(b)** Fitting analytical solution to the data collected at $z = L$ to find $\alpha$ $(cm^2/s)$ and $\beta$.

In the PLA-Air results shown in Figure 9, the gyroid structure has the highest thermal conductivity with 0.099 W/(m K), followed by cylindrical q-direction with thermal conductivity of 0.094 W/(m K). The cylindrical r-direction has a thermal conductivity of 0.073 W/(m K), and the lamellar structure has 0.072

W/(m K). These results show the importance of the continuity and complex structure of gyroid which had the highest thermal conductivity. Focusing on the comparison of the q- and r-directions in cylindrical samples, we see that the difference between these two directions is highly sensitive to which phase has higher thermal conductivity but is much less sensitive to the magnitude of the thermal conductivity ratio. It is worth mentioning that the harmonic average prediction for series orientation (equation 8, 0.044 W/(m K)) is lower than the measured thermal conductivity of all PLA-Air structures due, possibly, to natural convection in the air phase. For the PLA-Air lamellar samples in series orientation, the phases are not continuous, except through the PLA frame, which would likely require a 3D model to accurately predict. In the PLA-Thermal Paste system, the harmonic prediction agrees with lamellar results while it underpredicts the cylindrical q-direction and it slightly overpredicts the r-direction. The disagreement between experimental results and model predictions is greater than the 8% uncertainty observed in calibration measurements. These results show that thermal conductivity prediction should account for the orientation and tortuosity of the cylindrical structure. In the Appendix, we develop the following equation for predicting thermal conductivity in r- and q-directions. The predicted values for PLA-Air shown in equation 11 compare well with the experimental values reported in Table S4 and Figure 9.

$$k_q = k_{\tau_q} + k_{series,q} = 0.093\frac{W}{m\,K}\,(\text{eq. } 11.a) \qquad k_r = k_{\tau_r} + k_{series,r} = 0.078\frac{W}{m\,K}\,(\text{eq. } 11.b)$$

As discussed in more detail in the Appendix, the predictions and experiments for PLA-Thermal Paste agree well qualitatively.

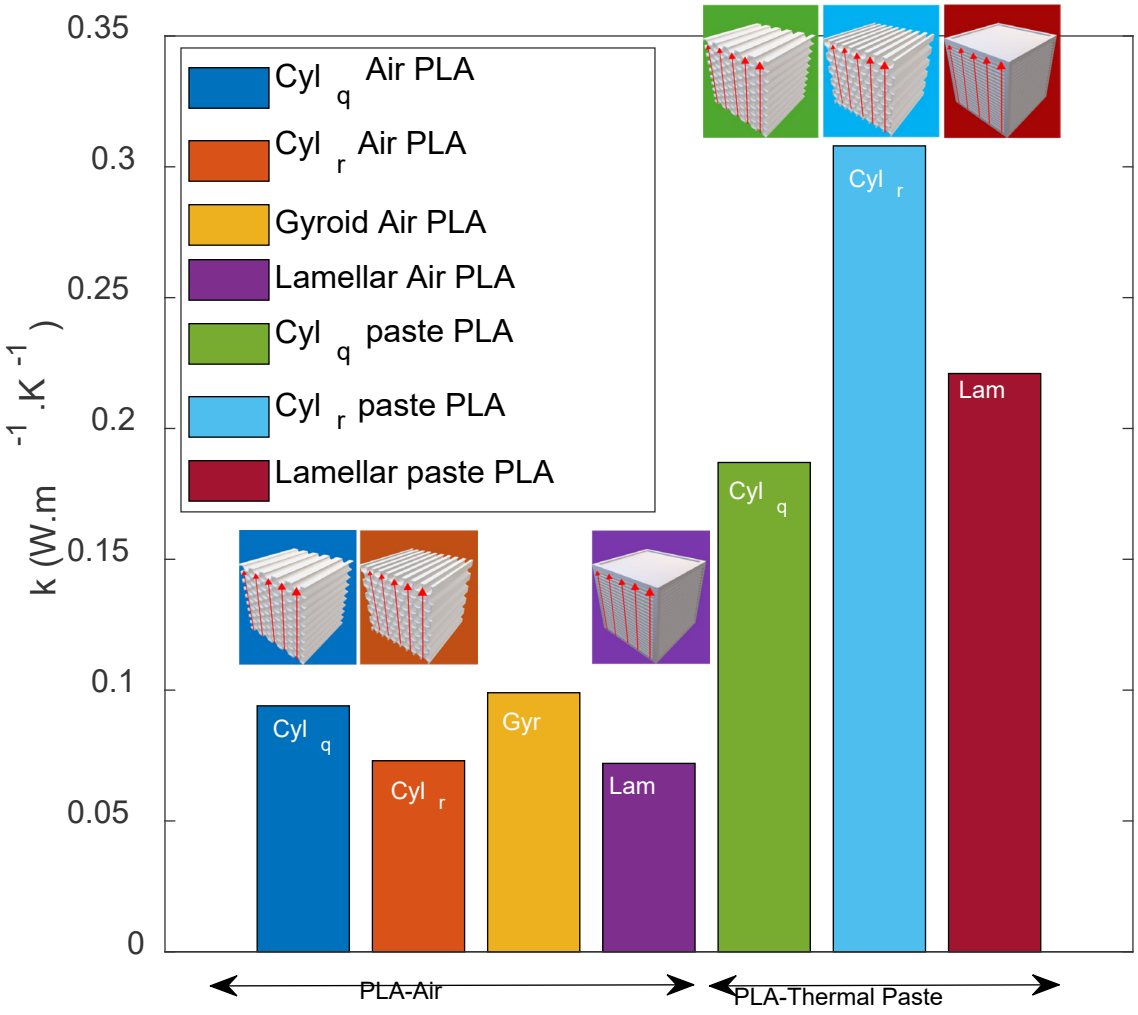


Figure 9. Thermal conductivity of each sample at 50% PLA volume from the steady-state series experiments. Cyl refers to cylindrical structure while q and r refer to axis directions in which heat conduction occurred. Gyr refers to gyroid structure, and Lam refers to lamellar structure. The insets depict sample orientation with red arrows that refer to heat flux direction. Due to symmetry, a gyroid inset is unnecessary.

### *3.2.1 Gyroid*

The gyroid structure has a symmetrical geometric structure. Due to this continuous symmetrical structure, there is no difference between series and parallel experiments. Figure 10 shows the thermal conductivity from the transient method with different models that account for the tortuosity. The thermal conductivity of the gyroid falls between the series prediction equation 9 and parallel prediction equation 8. Figure 10 (a) shows a combined model in which the series and parallel prediction are weighted by a factor, $f$, as shown in equation 12.

$$k_{combined} = f\ k_{parallel} + (1 - f)\ k_{series}\ (\text{eq. } 12)$$

The equation is fitted to the gyroid data to find $f$. The weighting factor $f$ is 0.843 with an $R^2$ value of 0.994. This indicates that more than 80% of the heat flux is transported via parallel pathways. Figure 10 (b) shows the thermal conductivity prediction using a geometric mean as shown in equation 13.

$$k_{geometricmean} = {k_{parallel}}^{(1-v)} {k_{series}}^{v}\ (\text{eq. } 13)$$

From regression to gyroid data, $v$ has a value of 0.126 with an $R^2$ value of 0.994. Finally, Figure 10 (c) shows the combination of 2 models, equations 14.a and 14.b, where the parallel and series pathways are adjusted to account for tortuosity rather than using a weighting factor.

$$k_{gyr-parallel} = \frac{5}{8}\phi_A k_A + \phi_B k_B\ (\text{eq. } 14.a)$$

$$k_{gyr-series} = \left(\frac{\frac{4}{5}\phi_A}{k_A} + \frac{\phi_B}{k_B}\right)^{-1}\ (\text{eq. } 14.b)$$

Phase A in equation 14 is the phase with lower thermal conductivity. In the PLA-Air system, phase A is Air. The 5/8 in equation 14.a resulted from regression to the data at high volume percentages. This value accounts for the tortuosity in the parallel direction of gyroid structure. The 4/5 in equation 14.b was chosen based on simulations by Shen and coworkers [63], in addition to the tortuosity effects described by Hallinan and coworkers. [22] In this tortuosity-based model, we take the expression with higher thermal conductivity at a given volume percentage, which is shown as the solid line/curve in Figure 10 (c). This assumes that heat will be transported exclusively through the more conductive pathway. The best fitting gyroid model is the tortuosity-based parallel/series combination model, equations 14.a and 14.b. Below 17% PLA volume, it follows equation 14.b, i.e. gyroid series. Above 17% PLA volume, the model follows equation 14.a, i.e. gyroid parallel. The other two models are also viable for predicting gyroid thermal conductivity, as they exhibit similar performance indicated by their equal $R^2$ values.

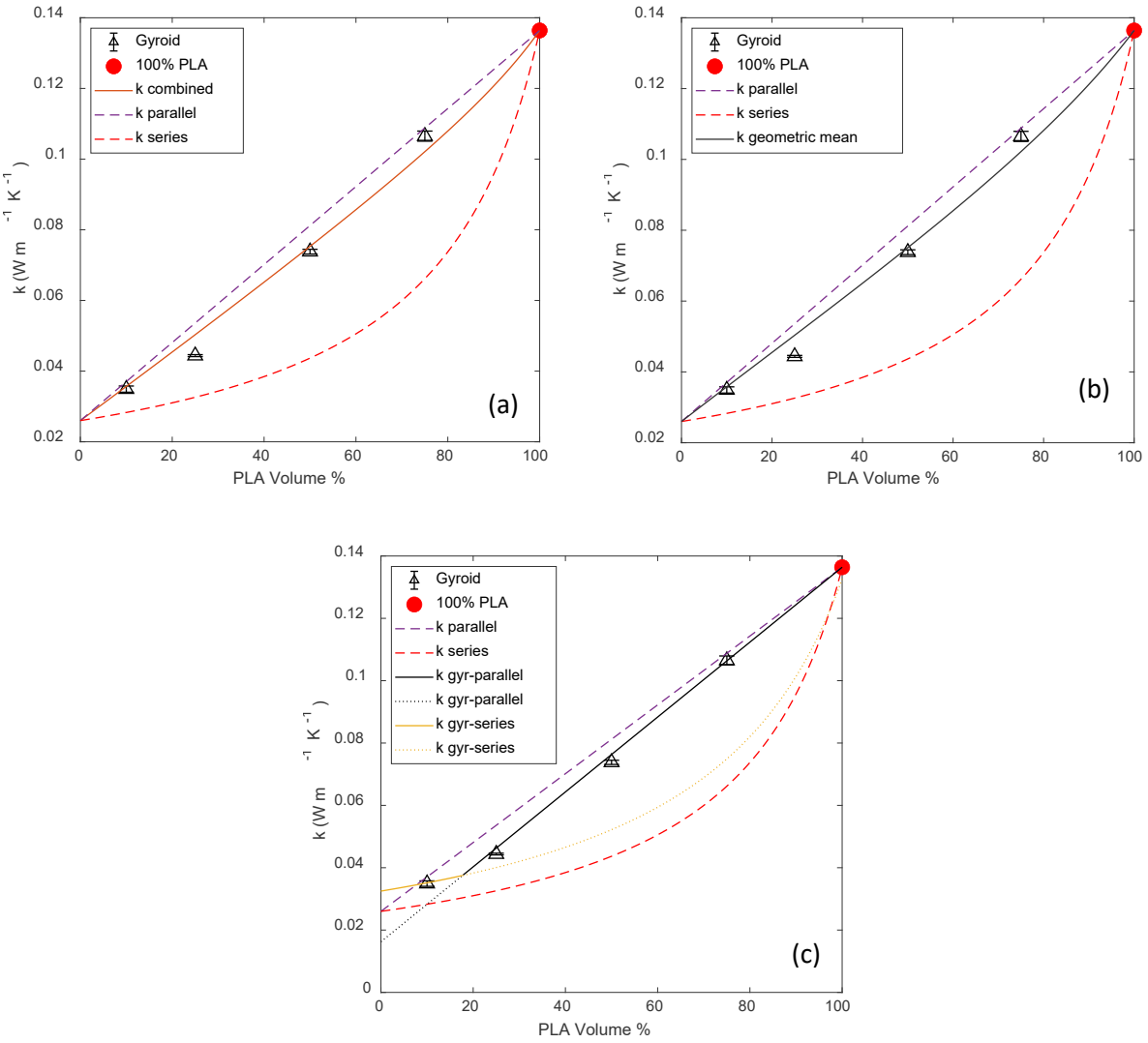


Figure 10. Gyroid structure thermal conductivity measurements using the transient method, along with different models for gyroid thermal conductivity. (a) combined model of series and parallel; (b) geometric mean prediction model; (c) tortuosity-based parallel/series combination model.

### *3.2.2 Discussion*

Many different approaches to modeling transport in complex structures have been developed. For example, a numerical finite-difference model for 2D transient diffusion in lamellar structures was developed by Taleb et al. The numerical results were compared to different theories such as effective medium theory and geometric mean. [23] This model can be utilized to analyze thermal transport, ion transport, and molecular diffusion. The model focused on assessing the impact of grain size, grain boundaries, and thermal conductivity ratio on apparent transport parameters. [23] Shen et al. studied diffusion in lamellae, cylinders, and double gyroid BCP nanostructures using random walks and coarse-

grained simulations, where they found the lamellae is most preferable for transport. [63] Luo et al. used the lattice Boltzmann method to investigate fluid flow, diffusion, and heat transfer inside reconstructed porous gyroid structures. [64] Overall, these studies largely utilize simulation and/or mathematical approaches to predict the thermal conductivity of different structures. Each study focuses on specific aspects such as shape or material composition. In the current work the impact of geometric structures including lamellar, cylindrical, and gyroid, alongside variations in volume percentage of PLA and thermal conductivity ratio have all been considered. Unlike previous studies that have predominantly focused on individual geometric structures or limited infill materials, in our experimental design, the utilization of 3D-printed PLA samples offers a unique platform to explore the interplay between geometric structure, volume percentage, and material combination on thermal conductivity.

In an effort to look for a universal way to capture the various effects of materials, structure, and volume fraction in co-continuous structures, the thermal conductivity is normalized between 0 and 1, using $\frac{k-k_n}{k_c-k_n}$, where $k$ is the thermal conductivity measured from the transient method for each sample, $k_n$ is the thermal conductivity of the less conductive phase, $\text{and } k_c$ is the thermal conductivity of the more conductive phase. This normalized conductivity is plotted as a function of the conductive phase volume fraction, $\phi_c$, in Figure 11. At extreme volume fractions of 0.1 and 0.75, structures and material combination play almost no role in normalized thermal conductivity value, indicated by the data points in Figure 11 being coincident. In contrast at $\phi_c$ values of 0.25 and 0.5, lamellar has the most conductive structure followed by gyroid and finally cylindrical structures. The result of a linear regression to the normalized data is shown in equation 15.

$$\frac{k-k_n}{k_c-k_n} = 1.028 \times \phi_c - 0.0368 \text{ (eq. 15)}$$

The universal values of this empirical fit provide a simple prediction that accounts for the dominant effects of volume fraction and material combination. With the exception of cylindrical PLA-Air, which is an outlier due to surface roughness, all investigated structures are reasonably well predicted by this simple empirical model. This indicates that it can be generalized and applied to other structures and novel systems not included in this study with thermal conductivity ratio, $\frac{k_c}{k_n} \leq 36$. It is unclear if the same trends will be observed at thermal conductivity ratios of 100, 1,000, or even 10,000.

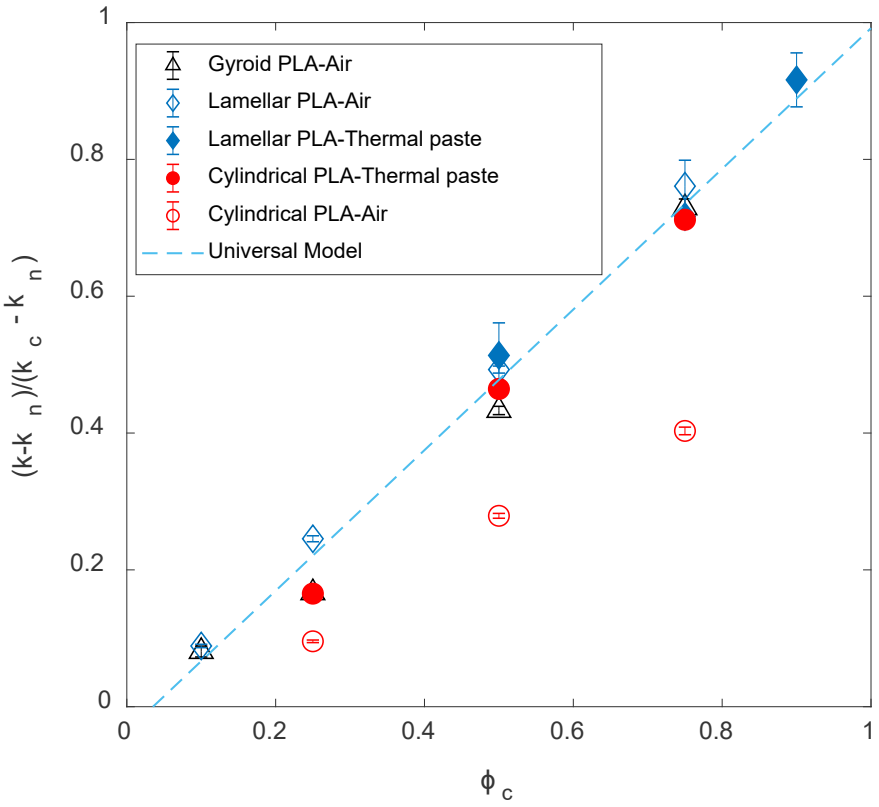


Figure 11. The normalization of thermal conductivity of different systems and structures relative to the volume fraction of the most conductive phase in the system.

### 3.3 Conclusions

Thermal conductivity of 3D-printed PLA structures was investigated with different materials and varying volume percentages. The study provided valuable insight into the effect of geometric shape, thermal conductivity ratio, and phase volume fraction on effective thermal conductivity. The experimental results for lamellar samples aligned closely with the theoretical models. In series orientation, the gyroid structures displayed enhanced thermal conductivity, attributed to their unique geometry providing efficient heat transfer pathways. Therefore, gyroid specific models were developed and tested. The thermal conductivity of cylindrical PLA-Air samples was significantly lower than all other structures due to a combination of surface roughness and inherently lower transport in hexagonally packed cylinders. The latter was proven by tests on cylindrical PLA-Thermal Paste samples. In steady-state series experiments, a key consideration was the orientation of the cylindrical structure relative to the heat source.

Future research should focus on modeling more complex structures and exploring higher $\frac{k_A}{k_B}$ ratios to uncover additional insights into heat transport phenomena. Experimental investigation of block copolymer inspired structures through 3D-printing techniques provides valuable data to enhance material modeling and simulations. In addition, a universal model has been developed to predict the thermal conductivity in any co-continuous structure with a thermal conductivity ratio of $\frac{k_c}{k_n} \leq 36$. Understanding the thermal

conductivity of different infill materials and geometries allows for the development of accurate predictive models, aiding in the design of advanced materials and structures for various applications. Such insights are of immense importance in fields like electronics cooling, energy efficiency, thermal simulations, and additive manufacturing. By harnessing the potential of block-copolymer-inspired, 3D-printed structures and their tailored thermal properties, we can drive technological advancements, create more sustainable solutions, and revolutionize multiple sectors reliant on efficient heat management.

## Acknowledgments

This work was supported by NSF CAREER award number 1751450. NSH would like to acknowledge partial support by the US Department of Energy, Office of Energy Efficiency and Renewable Energy, Advanced Manufacturing Office, under contract DE-AC05-00OR22725 with UT-Battelle, LLC. We thank Dr. Jonas Gustavsson for assistance with collecting sample photos.

## Appendix

**Derivation of Equation 11**

As can be seen in Figure 7, the heat has 2 possible pathways in the q and r directions to cross through the cube, which is either a tortuous pathway through the PLA phase alone, and/or a series pathway through PLA and air phases.

Tortuosity, $\tau$, must be considered in the first path and is defined as the effective path length that the heat travels, $L_{eff}$, normalized to the straight-line distance.

$$\tau \equiv \frac{L_{eff}}{L}$$
$$L_{eff} = C + \pi RN$$

$C = N\ a$ is the total distance of small steps $a$ (see Figure 7). $N$ is the total number of cylinders along the path in the direction of interest (q or r). The length of the series path, $L$, is

$$L = C + 2RN = 4\ cm$$

$$C = L - 2RN$$

$$L_{eff} = L - 2RN + \pi RN$$

$$L_{eff} = L + RN(\pi - 2)$$

Inserting the expressions for $L$ and $L_{eff}$ into the definition of tortuosity yields the following.

$$\tau = \frac{L + RN(\pi - 2)}{L}$$

Each value of $R = 1.8$ cm and $N$ are used in the tortuosity equation above for each direction, $N = 7$ for the q-direction and $N = 4$ for the r-direction. This gives the maximum tortuosity in each direction.

$$\tau_{q,max} = 4.6$$

$$\tau_r = 3.05$$

Tortuousity is more or less constant in the r-direction, but varies considerably by linecut in the q-direction. The minimum tortuosity in the q-direction is when $N = 0$,

$$\tau_{q,min} = 1$$

The averaged tortuosity of the q-direction is

$$\langle \tau_q \rangle = \frac{4.6 + 1}{2} = 2.8$$

$$\langle \tau_r \rangle = 3.05$$

The calculated thermal conductivity from tortuosity effect when choosing the first path is

$$k_{\tau_q} = \frac{1}{\langle \tau_q \rangle} k_{PLA}$$

$$k_{\tau_r} = \frac{1}{\langle \tau_r \rangle} k_{PLA}$$

Since heat can be conducted through both pathways simultaneously, the tortuosity expressions are combined with the series model (that is here weighted by the cross-sectional area fraction of each phase). The following equations complete the derivation of a Cylindrical Composite Model, with values given for PLA-Air.

$\phi_{PLA,q} = \frac{g_q}{D} = 0.5 = \phi_{overall}$

$k_{series,q} = \left( \frac{\phi_{PLA,q}}{k_{PLA}} + \frac{(1-\phi_{PLA,q})}{k_{Air}} \right)^{-1}$

$k_{series,q} = 0.044 \frac{W}{m\,K}$

$k_{\tau_q} = \frac{1}{\langle \tau_q \rangle} k_{PLA} = 0.049 \frac{W}{m\,K}$

$k_q = k_{\tau_q} + k_{series,q} = 0.093 \frac{W}{m\,K}$

$k_{q,experimental} = 0.094$

$\phi_{PLA,r} = \frac{g_r}{D} = 0.25 = \frac{\phi_{overall}}{2}$

$k_{series,r} = \left( \frac{\phi_{PLA,r}}{k_{PLA}} + \frac{(1-\phi_{PLA,r})}{k_{Air}} \right)^{-1}$

$k_{series,r} = 0.033 \frac{W}{m\,K}$

$k_{\tau_r} = \frac{1}{\langle \tau_r \rangle} k_{PLA} = 0.045 \frac{W}{m\,K}$

$k_r = k_{\tau_r} + k_{series,r} = 0.078 \frac{W}{m\,K}$

$k_{r,experimental} = 0.073$

The same equations can be used for PLA-Thermal Paste (replacing $k_{Air}$ with $k_{paste}$), which results in the following values for the two series cylinder directions.

$k_{series,q} = 0.2657 \frac{W}{m\,K}$

$k_q = k_{\tau_q} + k_{series,q} = 0.3147 \frac{W}{m\,K}$

$k_{q,experimental} = 0.1807$

$k_{series,r} = 0.5051 \frac{W}{m\,K}$

$k_r = k_{\tau_r} + k_{series,r} = 0.5501 \frac{W}{m\,K}$

$k_{r,experimental} = 0.308$

Although the model and measurements do not agree quantitatively in this case, the qualitative trends do agree, that the r-direction is 70% to 80% greater than the q-direction when the cylinders are the more conductive phase. It is possible that the discrepancy between model and data is due to imperfect filling of the cylinders with the viscous thermal paste.

# References

[1] E.S. Toberer, L.L. Baranowski, C. Dames, Advances in thermal conductivity, Annual Review of Materials Research, 42 (2012) 179-209.
[2] X.-h. Qu, L. Zhang, W. Mao, S.-b. Ren, Review of metal matrix composites with high thermal conductivity for thermal management applications, Progress in Natural Science: Materials International, 21(3) (2011) 189-197.
[3] M. Vadivelu, C.R. Kumar, G.M. Joshi, Polymer composites for thermal management: a review, Composite Interfaces, 23(9) (2016) 847-872.
[4] M. Chen, S. Zhang, L. Zhao, J. Weng, D. Ouyang, Q. Chen, Q. Kong, J. Wang, Preparation of thermally conductive composite phase change materials and its application in lithium-ion batteries thermal management, Journal of Energy Storage, 52 (2022) 104857.
[5] Y.-N. Song, M.-Q. Lei, D.-L. Han, Y.-C. Huang, S.-P. Wang, J.-Y. Shi, Y. Li, L. Xu, J. Lei, Z.-M. Li, Multifunctional membrane for thermal management applications, ACS Applied Materials & Interfaces, 13(16) (2021) 19301-19311.
[6] Z. Han, A. Fina, Thermal conductivity of carbon nanotubes and their polymer nanocomposites: A review, Prog. Polym. Sci., 36(7) (2011) 914-944.
[7] F. Tian, Z. Ren, High thermal conductivity in boron arsenide: from prediction to reality, Angewandte Chemie, 131(18) (2019) 5882-5889.
[8] J. Chen, X. Huang, B. Sun, P. Jiang, Highly thermally conductive yet electrically insulating polymer/boron nitride nanosheets nanocomposite films for improved thermal management capability, ACS nano, 13(1) (2018) 337-345.
[9] S. Mallik, N. Ekere, C. Best, R. Bhatti, Investigation of thermal management materials for automotive electronic control units, Applied Thermal Engineering, 31(2-3) (2011) 355-362.
[10] S.J. Pety, M.H.Y. Tan, A.R. Najafi, P.R. Barnett, P.H. Geubelle, S.R. White, Carbon fiber composites with 2D microvascular networks for battery cooling, International Journal of Heat and Mass Transfer, 115 (2017) 513-522.
[11] K.M. Razeeb, E. Dalton, G.L.W. Cross, A.J. Robinson, Present and future thermal interface materials for electronic devices, International Materials Reviews, 63(1) (2018) 1-21.
[12] X.M. Sun, H. Sun, H.P. Li, H.S. Peng, Developing Polymer Composite Materials: Carbon Nanotubes or Graphene?, Advanced Materials, 25(37) (2013) 5153-5176.
[13] F. Zhang, Y.Y. Feng, W. Feng, Three-dimensional interconnected networks for thermally conductive polymer composites: Design, preparation, properties, and mechanisms, Materials Science & Engineering R-Reports, 142 (2020).
[14] Y. Mai, A. Eisenberg, Self-assembly of block copolymers, Chem. Soc. Rev., 41(18) (2012) 5969-5985.
[15] A.J. Meuler, M.A. Hillmyer, F.S. Bates, Ordered Network Mesostructures in Block Polymer Materials, Macromolecules, 42(19) (2009) 7221-7250.
[16] M.W. Matsen, F.S. Bates, Unifying weak- and strong-segregation block copolymer theories, Macromolecules, 29(4) (1996) 1091-1098.
[17] E.W. Cochran, C.J. Garcia-Cervera, G.H. Fredrickson, Stability of the gyroid phase in diblock copolymers at strong segregation, Macromolecules, 39(7) (2006) 2449-2451.
[18] Y. Kambe, C.G. Arges, S. Patel, M.P. Stoykovish, P.F. Nealey, Ion conduction in microphase-separated block copolymer electrolytes, The Electrochemical Society Interface, 26(1) (2017) 61.
[19] C. Zhai, H. Zhou, T. Gao, L. Zhao, S. Lin, Electrostatically tuned microdomain morphology and phase-dependent ion transport anisotropy in single-ion conducting block copolyelectrolytes, Macromolecules, 51(12) (2018) 4471-4483.

[20] C.G. Arges, Y. Kambe, M. Dolejsi, G.-P. Wu, T. Segal-Pertz, J. Ren, C. Cao, G.S. Craig, P.F. Nealey, Interconnected ionic domains enhance conductivity in microphase separated block copolymer electrolytes, Journal of Materials Chemistry A, 5(11) (2017) 5619-5629.
[21] A. Mayer, D. Steinle, S. Passerini, D. Bresser, Block copolymers as (single-ion conducting) lithium battery electrolytes, Nanotechnology, 33(6) (2021) 062002.
[22] D.T. Hallinan, I. Villaluenga, N.P. Balsara, Polymer and composite electrolytes, MRS Bulletin, 43(10) (2018) 759-767.
[23] O. Taleb, D.C. Barzycki, C.G. Polanco, R.G. Ricarte, D. Hallinan, Assessing effective medium theories for conduction through lamellar composites, International Journal of Heat and Mass Transfer, 188 (2022) 122631.
[24] N. Mehra, L. Mu, T. Ji, X. Yang, J. Kong, J. Gu, J. Zhu, Thermal transport in polymeric materials and across composite interfaces, Applied Materials Today, 12 (2018) 92-130.
[25] S. Sharick, J. Koski, R.A. Riggleman, K.I. Winey, Isolating the Effect of Molecular Weight on Ion Transport of Non-Ionic Diblock Copolymer/Ionic Liquid Mixtures, Macromolecules, 49(6) (2016) 2245-2256.
[26] W.-S. Young, T.H. Epps, Ionic Conductivities of Block Copolymer Electrolytes with Various Conducting Pathways: Sample Preparation and Processing Considerations, Macromolecules, 45(11) (2012) 4689-4697.
[27] P.W. Majewski, M. Gopinadhan, W.-S. Jang, J.L. Lutkenhaus, C.O. Osuji, Anisotropic Ionic Conductivity in Block Copolymer Membranes by Magnetic Field Alignment, Journal of the American Chemical Society, 132(49) (2010) 17516-17522.
[28] R. Mäki-Ontto, K. de Moel, E. Polushkin, G. Alberda van Ekenstein, G. ten Brinke, O. Ikkala, Tridirectional Protonic Conductivity in Soft Materials, Adv. Mater., 14(5) (2002) 357-361.
[29] P.W. Majewski, M. Gopinadhan, C.O. Osuji, The Effects of Magnetic Field Alignment on Lithium Ion Transport in a Polymer Electrolyte Membrane with Lamellar Morphology, Polymers, 11(5) (2019) 887.
[30] K. Timachova, I. Villaluenga, L. Cirrincione, M. Gobet, R. Bhattacharya, X. Jiang, J. Newman, L.A. Madsen, S.G. Greenbaum, N.P. Balsara, Anisotropic Ion Diffusion and Electrochemically Driven Transport in Nanostructured Block Copolymer Electrolytes, The Journal of Physical Chemistry B, 122(4) (2018) 1537-1544.
[31] D.M. Smith, Q. Pan, S. Cheng, W. Wang, T.J. Bunning, C.Y. Li, Nanostructured, Highly Anisotropic, and Mechanically Robust Polymer Electrolyte Membranes via Holographic Polymerization, Advanced Materials Interfaces, 5(1) (2018) 1700861.
[32] V. Gupta, R. Krishnamoorti, J. Kornfield, S. Smith, Evolution of microstructure during shear alignment in a polystyrene-polyisoprene lamellar diblock copolymer, Macromolecules, 28(13) (1995) 4464-4474.
[33] V. Gupta, R. Krishnamoorti, Z. Chen, J. Kornfield, S. Smith, M. Satkowski, J. Grothaus, Dynamics of shear alignment in a lamellar diblock copolymer: Interplay of frequency, strain amplitude, and temperature, Macromolecules, 29(3) (1996) 875-884.
[34] W.-S. Young, T.H. Epps III, Ionic conductivities of block copolymer electrolytes with various conducting pathways: sample preparation and processing considerations, Macromolecules, 45(11) (2012) 4689-4697.
[35] A. Keller, E. Pedemonte, F. Willmouth, Macro lattice from segregated amorphous phases of a three block copolymer, Kolloid-Zeitschrift und Zeitschrift für Polymere, 238 (1970) 385-389.
[36] M.J. Park, N.P. Balsara, Anisotropic proton conduction in aligned block copolymer electrolyte membranes at equilibrium with humid air, Macromolecules, 43(1) (2010) 292-298.
[37] E. Verploegen, T. Zhang, N. Murlo, P.T. Hammond, Influence of variations in liquid-crystalline content upon the self-assembly behavior of siloxane-based block copolymers, Soft Matter, 4(6) (2008) 1279-1287.

[38] S. Chandran, J. Baschnagel, D. Cangialosi, K. Fukao, E. Glynos, L.M.C. Janssen, M. Müller, M. Muthukumar, U. Steiner, J. Xu, S. Napolitano, G. Reiter, Processing Pathways Decide Polymer Properties at the Molecular Level, Macromolecules, 52(19) (2019) 7146-7156.
[39] P.L. Zhang, X.R. Yang, X.L. Li, Y. Xie, S.T. Liu, J.C. Huang, Experimental study on an integrated system of thermosyphon loop and vapor compression assisted with phase change material for pulse heat load, Applied Thermal Engineering, 241 (2024).
[40] Z.P. Yang, S.M. Jia, Y.T. Niu, X.T. Lv, H.L. Fu, Y.Y. Zhang, D.P. Liu, B. Wang, Q.W. Li, Bean-Pod-Inspired 3D-Printed Phase Change Microlattices for Solar-Thermal Energy Harvesting and Storage, Small, 17(30) (2021).
[41] X.S. Hu, X.L. Gong, Experimental study on the thermal response of PCM-based heat sink using structured porous material fabricated by 3D printing, Case Studies in Thermal Engineering, 24 (2021).
[42] Y.J. Li, T.T. Gao, Z. Yang, C.J. Chen, W. Luo, J.W. Song, E. Hitz, C. Jia, Y.B. Zhou, B.Y. Liu, B. Yang, L.B. Hu, 3D-Printed, All-in-One Evaporator for High-Efficiency Solar Steam Generation under 1 Sun Illumination, Advanced Materials, 29(26) (2017).
[43] J.X. Shi, H.L. Chen, S.H. Jia, W.J. Wang, 3D printing fabrication of porous bismuth antimony telluride and study of the thermoelectric properties, Journal of Manufacturing Processes, 37 (2019) 370-375.
[44] Z.S. Wang, W. Cui, H. Yuan, X.L. Kang, Z. Zheng, W.B. Qiu, Q.J. Hu, J. Tang, X.D. Cui, Direct ink writing of Bi2Te3-based thermoelectric materials induced by rheological design, Materials Today Energy, 31 (2023).
[45] C.H. Song, J.M. Lee, D.D. Lim, W. Choi, Rationally Tunable Phase Change Material Thermal Properties Enabled by Three-Dimensionally Printed Structural Materials and Carbon-Based Functional Additives, International Journal of Energy Research, 2023 (2023).
[46] Y.E. Belarbi, F. Benmahiddine, A.E. Hamami, S. Guessasma, S. Belhabib, Hygrothermal and Microstructural Investigation of PLA and PLA-Flax Printed Structures, Fibers, 10(3) (2022).
[47] Q.N. Lv, Z.L. Peng, Y. Meng, H.R. Pei, Y.H. Chen, E. Ivanov, R. Kotsilkova, Three-Dimensional Printing to Fabricate Graphene-Modified Polyolefin Elastomer Flexible Composites with Tailorable Porous Structures for Electromagnetic Interference Shielding and Thermal Management Application, Industrial & Engineering Chemistry Research, 61(45) (2022) 16733-16746.
[48] D.M. Codorniu, J.J. Moyano, M. Belmonte, M.I. Osendi, P. Miranzo, Thermal conduction in three-dimensional printed porous samples by high resolution infrared thermography, Open Ceramics, 4 (2020).
[49] M. Belmonte, G. Lopez-Navarrete, M.I. Osendi, P. Miranzo, Heat dissipation in 3D printed cellular aluminum nitride structures, Journal of the European Ceramic Society, 41(4) (2021) 2407-2414.
[50] N.T. Trifale, E.A. Nauman, K. Yazawa, Systematic Generation, Analysis, and Characterization of 3D Micro-architected Metamaterials, ACS Applied Materials & Interfaces, 8(51) (2016) 35534-35544.
[51] C.A. Yang, W.C. Wu, Z. Fu, H.D. Zheng, Preparation and thermal insulation properties of TPMS 3Y-TZP ceramics using DLP 3D printing technology, Journal of Materials Science, 58(29) (2023) 11992-12007.
[52] G.P. Feng, G.F. Pan, Y.H. Feng, X.X. Zhang, L. Qiu, Topology optimization of controllable porous microstructure with maximum thermal conductivity, International Journal of Heat and Mass Transfer, 220 (2024).
[53] B. Grabowska, J. Kasperski, The Thermal Conductivity of 3D Printed Plastic Insulation Materials—The Effect of Optimizing the Regular Structure of Closures, Materials, 13(19) (2020) 4400.
[54] Y. Yang, Z.Y. Wang, Q.Q. He, X.J. Li, G.X. Lu, L.M. Jiang, Y.S. Zeng, B. Bethers, J. Jin, S. Lin, S.Q. Xiao, Y.Z. Zhu, X.K. Wu, W.W. Xu, Q.M. Wang, Y. Chen, 3D Printing of Nacre-Inspired Structures with Exceptional Mechanical and Flame-Retardant Properties, Research, 2022 (2022).
[55] M. Mehrpouya, H. Vahabi, S. Janbaz, A. Darafsheh, T.R. Mazur, S. Ramakrishna, 4D printing of shape memory polylactic acid (PLA), Polymer, 230 (2021) 124080.
[56] Y. Xia, Y. He, F. Zhang, Y. Liu, J. Leng, A review of shape memory polymers and composites: mechanisms, materials, and applications, Advanced materials, 33(6) (2021) 2000713.

[57] L. Sun, T.X. Wang, H.M. Chen, A.V. Salvekar, B.S. Naveen, Q. Xu, Y. Weng, X. Guo, Y. Chen, W.M. Huang, A brief review of the shape memory phenomena in polymers and their typical sensor applications, Polymers, 11(6) (2019) 1049.
[58] J.-N. Shi, M.-D. Ger, Y.-M. Liu, Y.-C. Fan, N.-T. Wen, C.-K. Lin, N.-W. Pu, Improving the thermal conductivity and shape-stabilization of phase change materials using nanographite additives, Carbon, 51 (2013) 365-372.
[59] M.C. George, M.A. Rodriguez, M.S. Kent, G.L. Brennecka, P.E. Hopkins, Thermal conductivity of self-assembling symmetric block copolymer thin films of polystyrene-block-poly (methyl methacrylate), Journal of Heat Transfer, 138(2) (2016) 024505.
[60] I. Blanco, G. Cicala, G. Recca, C. Tosto, Specific Heat Capacity and Thermal Conductivity Measurements of PLA-Based 3D-Printed Parts with Milled Carbon Fiber Reinforcement, Entropy, 24(5) (2022) 654.
[61] G. Spinelli, R. Kotsilkova, E. Ivanov, V. Georgiev, C. Naddeo, V. Romano, Thermal and Dielectric Properties of 3D Printed Parts Based on Polylactic Acid Filled with Carbon Nanostructures, in: Macromolecular Symposia, Wiley Online Library, 2022, pp. 2100244.
[62] E.W. Lemmon, R.T. Jacobsen, Viscosity and thermal conductivity equations for nitrogen, oxygen, argon, and air, International journal of thermophysics, 25 (2004) 21-69.
[63] K.-H. Shen, J.R. Brown, L.M. Hall, Diffusion in lamellae, cylinders, and double gyroid block copolymer nanostructures, ACS Macro Letters, 7(9) (2018) 1092-1098.
[64] J.-W. Luo, L. Chen, T. Min, F. Shan, Q. Kang, W. Tao, Macroscopic transport properties of Gyroid structures based on pore-scale studies: permeability, diffusivity and thermal conductivity, International Journal of Heat and Mass Transfer, 146 (2020) 118837.